The Cryosphere, 13, 2043–2049, 2019
https://doi.org/10.5194/tc-13-2043-2019

The Cryosphere Open Access EGU

Brief communication: Updated GAMDAM glacier inventory over high-mountain Asia

Akiko Sakai

Graduate School of Environmental Studies, Nagoya University, Nagoya, Japan

Correspondence: Akiko Sakai (shakai@nagoya-u.jp)

Received: 4 July 2018 – Discussion started: 20 July 2018
Revised: 9 June 2019 – Accepted: 24 June 2019 – Published: 19 July 2019

Abstract. The original Glacier Area Mapping for Discharge from the Asian Mountains (GAMDAM) glacier inventory was the first methodologically consistent dataset for high-mountain Asia. Nonetheless, the GAMDAM inventory underestimated glacier area, as it did not include steep ice- and snow-covered slopes or shaded components. During revision of the inventory, Landsat imagery free of shadow, cloud, and seasonal snow cover was selected for the period 1990–2010, after which $> 90\,\%$ of the glacier area was delineated. The updated GAMDAM inventory, comprised of 453 Landsat images, includes 134 770 glaciers with a total area of $100\,693 \pm 11\,790\,\mathrm{km}^2$.

1 Introduction

Glaciers in high-mountain Asia (HMA) play a significant role as a water resource for people living downstream (Immerzeel et al., 2010; Bolch et al., 2012). Glacier recession in recent decades has contributed to sea level rise, and this trend is anticipated to continue in the future (Huss and Hock, 2015; Marzeion et al., 2018; Radić and Hock, 2013). Recent analysis of surface elevation change has revealed that glaciers in HMA exhibit contrasting behaviour (Brun et al., 2017; Gardner et al., 2013; Kääb et al., 2012, 2015): those in the Himalaya and the eastern Nyainqêntanglha Mountains are shrinking rapidly, while the Karakoram and West Kunlun glaciers are in balance or show a slight mass gain. Accordingly, a recent climate analysis for those areas demonstrated that the Karakoram and West Kunlun regions are relatively stable under global warming conditions, being less sensitive to temperature change (Sakai and Fujita, 2017). This assessment of both glacier volume and climatic conditions is based on a large-scale glacier inventory, highlighting the need for accurate, high-quality coverage of the entire HMA region. Specifically, precise glacier inventories are needed for modelling total glacier volume (Frey et al., 2014; Farinotti et al., 2019), deriving volume change from altimetry and digital elevation maps (DEMs, e.g. Brun et al., 2017) and surface-flow velocity (Dehecq et al., 2019), establishing changes in snow cover and albedo (Naegeli et al., 2019), catchment- and regional-scale hydrologic modelling (e.g. Immerzeel et al., 2010), projecting future glacier configuration (Huss and Hock, 2015; Shannon et al., 2019), and assessing uncertainty in estimates of glacier-surface elevation change (e.g. Nuimura et al., 2012; Bolch et al., 2017).

While the Randolph Glacier Inventory (RGI) (Arendt et al., 2015; RGI Consortium, 2017) was the first database with global coverage, the record exhibits considerable variability in accuracy even within HMA. Regional databases include the second Chinese glacier inventory (hereafter the CGI2), produced by automatic delineation with manual correction (Guo et al., 2015), and the NM18 inventory for the Karakoram and Pamir region (Mölg et al., 2018), derived from automated digital mapping and corrected manually by the coherence of synthetic aperture radar (SAR) imagery for debris-covered glaciers (Frey et al., 2012). The latter study also made separate delineations for all debris-covered areas.

Between February 2011 and March 2014, the Glacier Area Mapping for Discharge from the Asian Mountains (GAMDAM) project compiled a glacier inventory for HMA, covering the region between 27.0 and 54.9° N in latitude and 67.4 and 103.9° E in longitude. In its first iteration, published in 2015, the GAMDAM glacier inventory (GGI) did not include steep ice- and snow-covered slopes. Moreover, where wintertime imagery was employed to avoid summer monsoon cloud

cover, shaded areas of glacier surfaces were excluded from the inventory (Fig. S1a in the Supplement). To help address these shortcomings, I present a revised glacier inventory for HMA based on summertime (May–September) imagery, exhibiting clear glacier boundaries for steep, snow-covered slopes and shaded areas. The abbreviated terms GGI15 and GGI18 refer to the first version of the GGI (Nuimura et al., 2015) and the current, updated version (this study), respectively.

2 Data

I utilized a total of 453 Landsat 5 Thematic Mapper™ and Landsat 7 Enhanced Thematic Mapper Plus (ETM+) level 1T scenes derived from 196 USGS EarthExplorer path–row sets (http://earthexplorer.usgs.gov/, last access: 17 July 2019). Landsat ID and acquisition dates were used to delineate glacier outlines and are summarized in Table S1 in the Supplement. Due to the challenge of obtaining summertime imagery for the 1999–2003 setting period (Nuimura et al., 2015) that is free of clouds, seasonal snow cover, and shadows, the annual search range was expanded to 1990–2010 and the monthly search range to May–September (i.e. the high-solar-angle season). Where part of a glacier surface was obscured by cloud or snow, the Landsat archive was searched for more viable images covering that particular site; for glaciers with steep headwalls, images were selected with the most clearly defined glacier outlines (full details of this methodological approach are given in Sect. 3). As a result, the GGI18, like its predecessor, contains single path–row scenes comprised of multiple images (Fig. 1). Finally, the GGI18 employs the ASTER-GDEM2 to analyse the glacier aspect in each 90 m × 90 m grid.

3 Methods

Unlike seasonal snow cover, glaciers are considered to be permanent snow and ice. It is vital, therefore, that seasonal snow coverage is excluded from each glacier polygon. In addition, to help quantify the glacial contribution to sea level change and water resources, polygons must include all areas in which fluctuations in surface elevation reflect changes in ice mass.

3.1 Selection of Landsat imagery

As detailed in Sect. 2, I expanded the search period to obtain Landsat images in which glacier outlines are depicted clearly. Figure S1, for example, shows the five images selected to delineate glacier outlines in the accumulation zone of the Khumbu Glacier, in the Nepalese Himalaya. While the cloud-free image in Fig. S1a was utilized for the GGI15, large areas of the glacier surface lie in shadow, thus precluding accurate delineation. Therefore, during revision for the

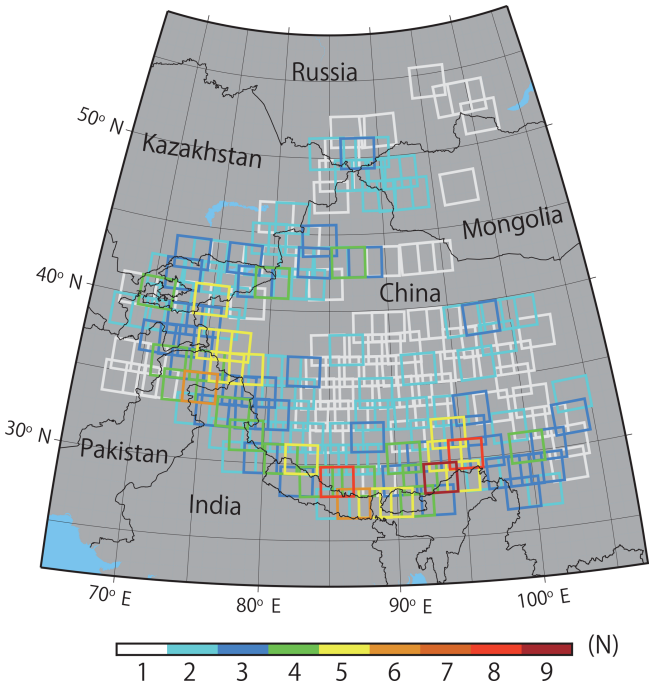

Figure 1. Footprints of the Landsat scenes used in the GGI18. Colours indicate the number of scenes used to delineate glacier outlines.

GGI18, I selected an additional two images (Fig. S1b and c) with minimal snow and no cloud cover over the target glaciers (Fig. S1). Focusing on the steep snow-covered headwalls of the Khumbu Glacier (purple ellipses in right panels, Fig. S1), the image displayed in Fig. S1b exhibits the least seasonal snow cover and provides the sharpest boundaries among the four additional images, and thus this was utilized in the GGI18.

Ultimately, the degrees of cloud and snow cover and the clarity of glacier outlines are the key factors in selecting suitable Landsat imagery for glacier delineation. The most challenging sites are those for which the glacier headwall comprises at least part of the accumulation area; to delineate such glaciers accurately, I focused on unambiguous boundaries on north-facing walls. Nonetheless, in regions dominated by summer monsoonal precipitation, such as the eastern Himalaya and eastern Nyainqêntanglha Mountains, the approach described here was inadequate to locate appropriate imagery (see Sect. 4.3).

3.2 Manual delineation

Owing to the many debris-covered glaciers in HMA (e.g. Herreid et al., 2015; Minora et al., 2016; Nagai et al., 2016; Ojha et al., 2017), for which automatic detection using the band ratio method is not possible (Paul et al., 2002), all glacier outlines included in the GGI18 were delineated manually. Using the newly selected Landsat imagery, I modified

the GGI15 glacier polygons following the method described by Nuimura et al. (2015) but with two important differences. First, whereas glaciers of $< 0.05\,km^2$ in area were excluded from the GGI15 (Nuimura et al., 2015), the minimum glacier area in the GGI18 is $0.01\,km^2$ so as to account for the numerous small glaciers separated by dividing ridges. Furthermore, I included small glaciers as much as possible during the revision process. A total of 10 grid cells ($= 0.009\,km^2$) were used as a guide for measuring area. In contrast to the GGI15, in which glacier outlines were delineated manually by 11 individuals (Nuimura et al., 2015), all of the delineation for the GGI18 was conducted by a single person.

The second methodological difference between the GGI15 and the GGI18 relates to steep headwalls. Nuimura et al. (2015) excluded steep snow- and ice-covered slopes from the GGI15, arguing that glaciers on high-angle headwalls generally do not undergo changes in surface elevation related to mass fluctuations. Those authors also underestimated the scale of upper glacier headwalls that are mantled with snow or ice. In contrast, since I was able to obtain comparatively distinct outlines for those glaciers with relatively thick ice on steep headwalls, the GGI18 includes the snow- or ice-covered parts of the glacier surface. For instance, Fig. S2a depicts the high-angle, avalanche-prone headwall of the Trakarding Glacier in 2016, on which hanging glaciers are clearly visible. Thanks to their distinct outlines, these features are also identifiable on the 1999 Landsat image (arrows, Fig. S2b), indicating that they are long-term components of the glacier system and thus need to be included in the inventory.

The correct distinction between debris-covered glaciers and rock glaciers is a challenge, as gradual transitions can exist under permafrost conditions (Mölg et al., 2018). Rock glaciers have terrain with ridges and furrow surface patterns (Bodin et al., 2010), while debris-covered glaciers have ponds surrounded by ice cliffs. Those detailed topographies were difficult to detect via Landsat imagery because of its relatively low resolution. Therefore, debris-covered areas were determined from high-resolution Google Earth imagery. Specifically, those portions of the glacier surface exhibiting rock-glacier-like topography (e.g. flow lobes) were identified visually and omitted (see Fig. S3). As for the debris-covered glaciers in the eastern Himalaya and eastern Nyainqêntanglha Mountains, crevassed surfaces can be detected even in the snow-covered glacier surface using high-resolution Google Earth imagery. For regions where high-resolution Google Earth imagery is unavailable (e.g. eastern Himalaya and eastern Nyainqêntanglha Mountains) or the glacier surface is obscured by seasonal snow cover (e.g. Karakoram and Pamir), I employed a combination of contours and surface–colour difference between glacier areas and glacier-free areas to delineate debris-covered glaciers.

3.3 Uncertainties in glacier area

Revision of glacier outlines and subsequent delineation testing were both performed by the author. Delineation tests were conducted on 10 debris-covered glaciers and 12 debris-free glaciers using a total of 10 Landsat images (listed in Table S4), which included shaded (winter), snow-covered, and partially cloud-covered scenes. Since fully cloud-obscured images were not used in the delineation process, I did not select such glacier outlines in the testing process. Furthermore, I did not utilize Google Earth imagery since the resolution is not regionally uniform throughout HMA (see Sect. 3.2). For each Landsat image, I created a single glacier outline and calculated the normalized standard deviation (NSD: standard deviation divided by average glacier area) for each glacier area (e.g. Fig. S4). For each area class, the NSD increases with decreasing glacier area (Fig. S5). Moreover, NSD values are higher for debris-covered glaciers than for debris-free glaciers (particularly for smaller glaciers), although the GGI18 does not classify debris-covered and debris-free glaciers.

The proportion of debris-covered glaciers in each area class in the eastern Himalaya (27.5–29.0° N, 85.0–92.0° E) (Ojha et al., 2017) (Fig. S6) was applied for all of the study areas (HMA), then they were used to calculate the number-weighted average NSD of glacier area for each glacier area class, including both debris and debris-free glaciers (Fig. S6). Here, the NSDs of the glacier area were assumed to be 15 % for smaller ($< 0.25\,km^2$) debris-free glaciers and 30 % for smaller ($< 2\,km^2$) debris-covered glaciers based on Fig. S5. NSD for all glaciers in Fig. S6 was assumed to be the uncertainty in glacier area for all types of glacier (including debris-covered and debris-free). Finally, the maximum NSD 19 % was found for glaciers of 1–2 km^2 in area (Fig. S6).

4 Results and discussion

The GGI15 reported a total glacier area of $91\,263 \pm 13\,689\,km^2$ (Nuimura et al., 2015), which included the combined area of holes in glacier polygons. Excluding polygon holes, I recalculated the total glacier area in the GGI15 as $87\,583 \pm 3137\,km^2$ (Table 1), while the GGI18 is comprised of 134 770 glaciers with a total area of $100\,693 \pm 11\,790\,km^2$ (Table 1). Hence, the total glacier area and glacier number for HMA are 13 % and 35 % greater in the GGI18 than in the GGI15, respectively.

4.1 Comparison with the GGI15

Following the region delimitation of RGI 6.0 (Arendt et al., 2015; RGI Consortium, 2017), the aggregated polygon files for the GGI18 are divided into four regions: Central Asia, South Asia (east), South Asia (west), and North Asia (limited by the Sayan and Altai mountains). Regional differences in glacier area among the GGI18, GGI15, and RGI 6.0 are

Table 1. Comparison of the GGI15 and GGI18 inventories in terms of the total glacier area, glacier area ratio based on summer imagery, and based on imagery acquired between 1999 and 2001.

	Minimum glacier area (km^2)	Total glacier area (km^2)	Total number of glaciers	Number of Landsat images employed	Glacier area based on summer (JJAS) images (%)	Glacier area based on images acquired from 1999 to 2001 (%)
GGI15 (Nuimura et al., 2015)	0.05	$87\,583 \pm 13\,137$	87 084	356	69	73
GGI18 (this study)	0.01	$100\,693 \pm 11\,790$	134 770	453	95	48

summarized in Table S2 (note that the RGI 6.0 incorporated part of the GGI15; RGI Consortium, 2017). For all regions, glacier area in the GGI18 is > 10 % greater than in the GGI15, with the greatest differences in eastern South Asia (+18 %) and western South Asia (+16 %). Both eastern and western South Asia cover portions of the high Himalaya, including abundant high-relief glaciated headwalls, indicating that the GGI15 underestimated glacier area most in shaded areas. In the present study, I replaced glacier outlines delineated from winter imagery (GGI15) with those based on summer imagery (GGI18), with the result that glacier area ratios based on summer images increased from 69 % to 95 % (Table 1). Figure 2 provides a comparison of a glacier outline included in both the GGI15 and GGI18 inventories. In the former, glacier delineation was based on low-solar-angle, heavily shaded imagery; in the latter, such areas have been substituted with delineations based on high-solar-angle imagery (Fig. S7).

Total glacier area in the GGI18 includes components on north-facing slopes (Fig. S8). However, the acquisition dates of the imagery are variable. For instance, the glacier area ratio derived from images acquired between 1999 and 2001 decreased from 73 % in the GGI15 to 48 % in the GGI18 (Table 1). For both inventories, glacier area distributions for specific acquisition dates (month and year) are compared and summarized in Fig. S9. Glaciers located in monsoon-dominated regions were delineated primarily from non-summer (January–May and October–December) imagery in the GGI15 (Fig. S9a and b), whereas the majority of the total glacier area (> 90 %: Table 1) was extracted from summer (June–September) Landsat imagery (Fig. S9c).

According to the area–elevation distributions shown in Fig. S10a, total glacier area between 5000 and 6000 m elevation is greater in the GGI18 than in the GGI15. While glacier area in the GGI18 is measurably larger across all area classes (Fig. S10c), the greatest increase in glacier number is observed for small ($< 0.0625\,km^2$) glaciers (Fig. S10b). Glacier polygons were aggregated for each $1^\circ \times 1^\circ$ grid based on the barycentre of each glacier polygon for each inventory to assess regional differences (see Fig. S10d). Compared with the GGI15, the GGI18 exhibits higher glacier-area values in all regions except the Tibetan Plateau (Fig. S10d), where the general absence of high-relief terrain minimizes the magnitude of topographic shading.

4.2 Comparison with the CGI2 and NM18 inventories

To assess the GGI18 relative to the CGI2 (Guo et al., 2015) and NM18 (Mölg et al., 2018) inventories, I extracted the two components of the GGI18 covered by the respective domains of the other datasets. A direct comparison of the three reveals that the GGI18-derived glacier area is smaller than that of the CG12 for elevations of 4000–5500 m (Fig. S11a) and lower than that of the NM18-derived estimate for elevations of 4500–6000 m (Fig. S12a). In contrast, the GGI18 reports a greater number of smaller glaciers than the CG12 and the NM18, and larger glaciers comprise a smaller total area in the GGI18 (Figs. S11b, c and S12b, c). This pattern is likely due to the greater division in the GGI18 of large ice masses into multiple glaciers relative to the NM18 and CGI2.

For each $1^\circ \times 1^\circ$ grid cell, glacier polygons for all three inventories were aggregated based on the polygon barycentre, thereby enabling regional differences to be calculated (Figs. S11d and S12d). According to this comparison, glacier areas provided by the GGI18 and CG12 are regionally consistent (Fig. S11d), with the exception of the Nyainqêntanglha Mountains, for which the CGI2 was not updated following the first Chinese glacier inventory. In contrast, compared to the NM18, the GGI18 prescribes a slightly smaller glacier area for most regions (Fig. S12d). This disparity is potentially linked to the inclusion of seasonal snow in the NM18, due to the automatic band-ratio method employed over debris-free zones (Mölg et al., 2018), whereas the GGI18 tends to omit such small glaciers. Finally, I evaluated the degree of consistency between the GGI18 and the other two inventories using an overlapping ratio. This assessment provided an overlapping ratio of 87 % for the GGI18 and NM18, and a ratio of 86 % for the GGI18 and CGI2 to the total GGI18 over their respective domains (NM18/CGI2) (Table S3), indicating a high degree of consistency among the three inventories.

4.3 Glacier outlines requiring further revision

Clouds, seasonal snow cover, and strong shadows all hamper the detection of glacier outlines from Landsat imagery. Consequently, the number of scenes required to delineate glacier outlines for each path–row varies widely (Fig. 1), with monsoon-dominated regions utilizing the most imagery. Example of glacier outlines within such a limited area delin-

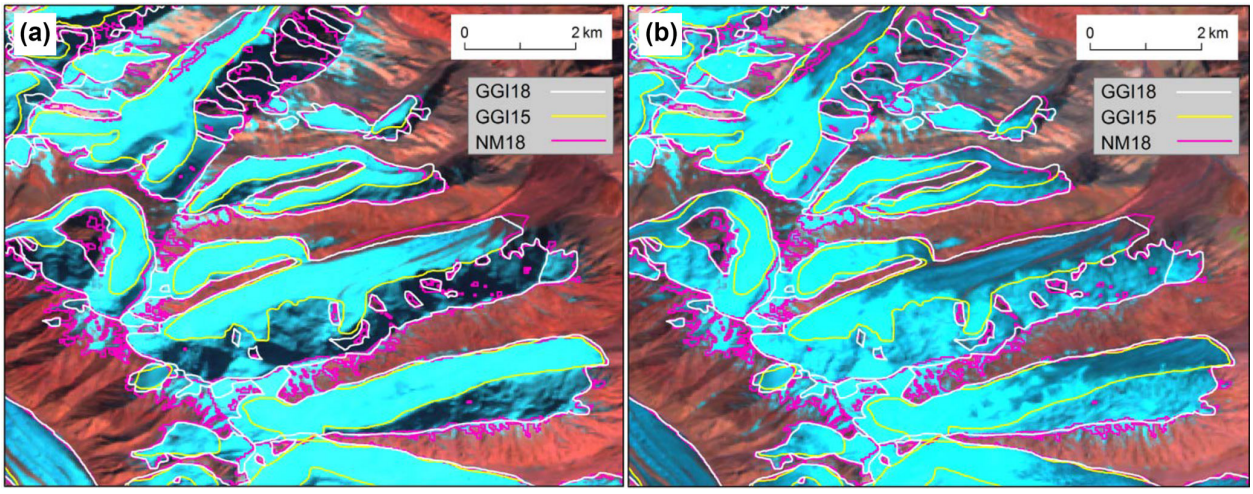

Figure 2. Comparison of glacier outlines used in the GGI15, GGI18, and NM18 inventories at 38.9236° N, 72.4217° E (path 151, row 33 of WRS2). Backgrounds are false-colour (bands 7, 4, and 2 as RGB) composite Landsat images taken on 28 September 2001 **(a)** and 26 July 2001 **(b)**. Glacier outlines of the GGI15 (yellow lines) were delineated based on the strongly shaded image on the left, whereas those of the GGI18 (white lines) were delineated using the less-shaded image on the right. Glacier outlines of the NM18 (pink lines; Mölg et al., 2018) are also shown for comparison.

eated using multiple images were shown in Fig. S13. Therefore, the number of images in Fig. 1 represents the degree of delineation accuracy.

As satellite imagery that is cloud-free and has the least seasonal snow becomes available from existing sources other than Landsat in the future, the glacier outlines delineated here from multiple images need to be revisited and, if necessary, revised. Sentinel-2 imagery, for instance, might prove a suitable alternative owing to its high resolution and shorter acquisition interval (≤ 5 d) relative to Landsat.

5 Summary

The updated version of the GAMDAM glacier inventory, the GGI18, incorporates all of HMA and includes 134 770 glaciers covering $100\,693 \pm 11\,790\,\mathrm{km}^2$. Although nearly 95 % of the total glacier area was delineated from summer images, the acquisition date of source imagery varies widely. Relative to its predecessor (GGI15), the total glaciated area in HMA is ~ 15 % greater in the GGI18, due primarily to the inclusion of glaciated north-facing slopes. Owing to cloud, seasonal snow cover, and topographic shading, a number of path–row scenes required multiple Landsat images to delineate glacier outlines fully and thus should be revisited in the future as higher-quality imagery becomes available.

Data availability. Data can be downloaded from the following sources.

1. GAMDAM glacier inventory for high-mountain Asia: Area–altitude distribution for Central Asia, https://doi.org/10.1594/PANGAEA.891415 (Sakai, 2018a).
2. GAMDAM glacier inventory for high-mountain Asia: Area–altitude distribution for North Asia, https://doi.org/10.1594/PANGAEA.891416 (Sakai, 2018b).
3. GAMDAM glacier inventory for high-mountain Asia: Area–altitude distribution for South Asia East, https://doi.org/10.1594/PANGAEA.891417 (Sakai, 2018c).
4. GAMDAM glacier inventory for high-mountain Asia: Area–altitude distribution for South Asia West, https://doi.org/10.1594/PANGAEA.891418 (Sakai, 2018d).
5. GAMDAM glacier inventory for high-mountain Asia: Central Asia in ArcGIS (shapefile) format, https://doi.org/10.1594/PANGAEA.891419 (Sakai, 2018e).
6. GAMDAM glacier inventory for high-mountain Asia: North Asia in ArcGIS (shapefile) format, https://doi.org/10.1594/PANGAEA.891420 (Sakai, 2018f).
7. GAMDAM glacier inventory for high-mountain Asia: South Asia East in ArcGIS (shapefile) format, https://doi.org/10.1594/PANGAEA.891421 (Sakai, 2018g).
8. GAMDAM glacier inventory for high-mountain Asia: South Asia West in ArcGIS (shapefile) format, https://doi.org/10.1594/PANGAEA.891422 (Sakai, 2018h).

Supplement. The supplement related to this article is available online at: https://doi.org/10.5194/tc-13-2043-2019-supplement.

Competing interests. The author declares that there is no conflict of interest.

Acknowledgements. This project was supported by a grant from the Grants-in-Aid for Scientific Research (26257202) of the Japan Society for the Promotion of Science. I wish to thank all members of the GAMDAM project for their valuable support in producing the first version of the GAMDAM glacier inventory.

Financial support. This research has been supported by the Funding Program for Next Generation World-Leading Researchers (grant no. GR052).

Review statement. This paper was edited by Tobias Bolch and reviewed by Frank Paul and Wanqin Guo.

References

Arendt, A., Bliss, A., Bolch, T., Cogley, J. G., Gardner, A. S., Hagen, J.-O., Hock, R., Huss, M., Kaser, G., Kienholz, C., Pfeffer, W. T., Moholdt, G., Paul, F., Radić, V., Andreassen, L. M., Bajracharya, S., Barrand, N. E., Beedle, M., Berthier, E., Bhambri, R., Brown, I., Burgess, E. W., Burgess, D., Cawkwell, F., Chinn, T., Copland, L., Davies, B., Angelis, H. de, Dolgova, E., Earl, L., Filbert, K., Forester, R., Fountain, A. G., Frey, H., Giffen, B., Glasser, N. F., Guo, W., Gurney, S. D., Hagg, W., Hall, D., Haritashya, U. K., Hartmann, G., Helm, C., Herreid, S., Howat, I., Kapustin, G., Khromova, T. E., König, M., Kohler, J., Kriegel, D., Kutuzov, S., Lavrentiev, I., Le Bris, R., Liu, S., Lund, J., Manley, W., Marti, R., Mayer, C., Miles, E. S., Li, X., Menounos, B., Mercer, A., Mölg, N., Mool, P., Nosenko, G., Negrete, A., Nuimura, T., Nuth, C., Pettersson, R., Racoviteanu, A., Ranzi, R., Rastner, P., Rau, F., Raup, B., Rich, J., Rott, H., Sakai, A., Schneider, C., Seliverstov, Y., Sharp, M. J., Sigurðsson, O., Stokes, C. R., Way, R. G., Wheate, R., Winsvold, S., Wolken, G., Wyatt, F., and Zheltihyna, N.: Randolph Glacier Inventory – A Dataset of Global Glacier Outlines: Version 5.0: GLIMS Technical Report, Global Land Ice Measurement from Space, Colorado, USA, Digital Media, available at: http://www.glims.org/RGI/randolph50.html (last access: 17 July 2019), 2015.

Bodin, X., Rojas, F., and Brenning, A.: Status and evolution of the cryosphere in the Andes of Santiago (Chile, 33.5° S), Geomorphology, 118, 453–464, https://doi.org/10.1016/j.geomorph.2010.02.016, 2010.

Bolch, T., Kulkarni, A., Kaab, A., Huggel, C., Paul, F., Cogley, J. G., Frey, H., Kargel, J. S., Fujita, K., Scheel, M., Bajracharya, S., and Stoffel, M.: The state and fate of Himalayan glaciers, Science, 336, 310–314, https://doi.org/10.1126/science.1215828, 2012.

Bolch, T., Pieczonka, T., Mukherjee, K., and Shea, J.: Brief communication: Glaciers in the Hunza catchment (Karakoram) have been nearly in balance since the 1970s, The Cryosphere, 11, 531–539, https://doi.org/10.5194/tc-11-531-2017, 2017.

Brun, F., Berthier, E., Wagnon, P., Kääb, A., and Treichler, D.: A spatially resolved estimate of High Mountain Asia glacier mass balances, 2000–2016, Nat. Geosci., 10, 668–673, https://doi.org/10.1038/NGEO2999, 2017.

Dehecq, A., Gourmelen, N., Gardner, A. S., Brun, F., Goldberg., D., Neinow P. W., Berthier, E., Vincent, C., Wagnon, P., and Trouve, E.: Twenty-first century glacier slowdown driven by mass loss in High Mountain Asia, Nat. Geosci., 12, 22–27, https://doi.org/10.1038/s41561-018-0271-9, 2019.

Farinotti, D., Huss, M., Fürst, J. J., Landmann, J., Machguth, H., Maussion, F., and Pandit, A.: A consensus estimate for the ice thickness distribution of all glaciers on Earth, Nat. Geosci., 12, 168–173, 2019.

Frey, H., Paul, F., and Strozzi, T.: Compilation of a glacier inventory for the western Himalayas from satellite data: Methods, challenges, and results, Remote Sens. Environ., 124, 832–843, https://doi.org/10.1016/j.rse.2012.06.020, 2012.

Frey, H., Machguth, H., Huss, M., Huggel, C., Bajracharya, S., Bolch, T., Kulkarni, A., Linsbauer, A., Salzmann, N., and Stoffel, M.: Estimating the volume of glaciers in the Himalayan–Karakoram region using different methods, The Cryosphere, 8, 2313–2333, https://doi.org/10.5194/tc-8-2313-2014, 2014.

Gardner, A. S., Moholdt, G., Cogley, J. G., Wouters, B., Arendt, A. A., Wahr, J., Berthier, E., Hock, R., Pfeffer, W. T., Kaser, G., Ligtenberg, S. R. M., Bolch, T., Sharp, M. J., Hagen, J. O., van den Broeke, M. R., and Paul, F.: A reconciled estimate of glacier contributions to sea level rise: 2003 to 2009, Science, 340, 852–857, https://doi.org/10.1126/science.1234532, 2013.

Guo, W., Liu, S., Xu, J., Wu, L., Shangguan, D., Yao, X., Wei, J., Bao, W., Yu, P., Liu, Q., and Jiang, Z.: The second Chinese glacier inventory: Data, methods and results, J. Glaciol., 61, 357–372, https://doi.org/10.3189/2015JoG14J209, 2015.

Herreid, S., Pellicciotti, F., Ayala, A., Chesnokova, A., Kienholz, C., Shea, J., and Shrestha, A.: Satellite observations show no net change in the percentage of supraglacial debris-covered area in northern Pakistan from 1977 to 2014, J. Glaciol., 61, 524–536, https://doi.org/10.3189/2015JoG14J227, 2015.

Huss, M. and Hock, R.: A new model for global glacier change and sea-level rise, Front. Earth Sci., 3, 54, https://doi.org/10.3389/feart.2015.00054, 2015.

Immerzeel, W. W., van Beek, L. P. H., and Bierkens, M. F. P.: Climate change will affect the Asian water towers, Science, 328, 1382–1385, https://doi.org/10.1126/science.1183188, 2010.

Kääb, A., Berthier, E., Nuth, C., Gardelle, J., and Arnaud, Y.: Contrasting patterns of early twenty-first century glacier mass change in the Himalayas, Nature, 488, 495–498, https://doi.org/10.1038/nature11324, 2012.

Kääb, A., Treichler, D., Nuth, C., and Berthier, E.: Brief Communication: Contending estimates of 2003–2008 glacier mass balance over the Pamir–Karakoram–Himalaya, The Cryosphere, 9, 557–564, https://doi.org/10.5194/tc-9-557-2015, 2015.

Marzeion, B., Kaser, G., Maussion, F., and Champollion, N.: Limited influence of climate change mitigation on short-term glacier mass loss, Nat. Clim. Change, 8, 305–308, https://doi.org/10.1038/s41558-018-0093-1, 2018.

Minora, U., Bocchiola, D., D'Agata, C., Maragno, D., Mayer, C., Lambrecht, A., Vuillermoz, E., Senese, A., Compostella, C., Smiraglia, C., and Diolaiuti, G. A.: Glacier area stability in the Central Karakoram National Park (Pakistan) in 2001–2010, Prog. Phys. Geog., 40, 629–660, https://doi.org/10.1177/0309133316643926, 2016.

Mölg, N., Bolch, T., Rastner, P., Strozzi, T., and Paul, F.: A consistent glacier inventory for Karakoram and Pamir derived from Landsat data: distribution of debris cover and

mapping challenges, Earth Syst. Sci. Data, 10, 1807–1827, https://doi.org/10.5194/essd-10-1807-2018, 2018.

Naegeli, K., Huss, M., and Hoelzle, M.: Change detection of bare-ice albedo in the Swiss Alps, The Cryosphere, 13, 397–412, https://doi.org/10.5194/tc-13-397-2019, 2019.

Nagai, H., Fujita, K., Sakai, A., Nuimura, T., and Tadono, T.: Comparison of multiple glacier inventories with a new inventory derived from high-resolution ALOS imagery in the Bhutan Himalaya, The Cryosphere, 10, 65–85, https://doi.org/10.5194/tc-10-65-2016, 2016.

Nuimura, T., Fujita, K., Yamaguchi, S., and Sharma, R. R.: Elevation changes of glaciers revealed by multitemporal digital elevation models calibrated by GPS survey in the Khumbu region, Nepal Himalaya, 1992–2008, J. Glaciol., 58, 648–656, https://doi.org/10.3189/2012JoG11J061, 2012.

Nuimura, T., Sakai, A., Taniguchi, K., Nagai, H., Lamsal, D., Tsutaki, S., Kozawa, A., Hoshina, Y., Takenaka, S., Omiya, S., Tsunematsu, K., Tshering, P., and Fujita, K.: The GAMDAM glacier inventory: a quality-controlled inventory of Asian glaciers, The Cryosphere, 9, 849–864, https://doi.org/10.5194/tc-9-849-2015, 2015.

Ojha, S., Fujita, K., Sakai, A., Nagai, H., and Lamsal, D.: Topographic controls on the debris-cover extent of glaciers in the Eastern Himalayas: Regional analysis using a novel high-resolution glacier inventory, Quatern. Int., 455, 82–92, https://doi.org/10.1016/j.quaint.2017.08.007, 2017.

Paul, F., Kääb, A., Maisch, M., Kellenberger, T., and Haeberli, W.: The new remote-sensing-derived Swiss glacier inventory: I. Methods, Ann. Glaciol., 34, 355–361, https://doi.org/10.3189/172756402781817941, 2002.

Radić, V. and Hock, R.: Glaciers in the Earth's hydrological cycle: Assessments of glacier mass and runoff changes on global and regional scales, Surv. Geophys., 3, 1–25, https://doi.org/10.1007/s10712-013-9262-y, 2013.

RGI Consortium: Randolph Glacier Inventory 6.0, available at: https://www.glims.org/RGI/ (last access: 17 July 2019), 2017.

Sakai, A.: GAMDAM glacier inventory for High Mountain Asia: Area–altitude distribution for Central Asia, https://doi.org/10.1594/PANGAEA.891415, 2018a.

Sakai, A.: GAMDAM glacier inventory for High Mountain Asia: Area–altitude distribution for North Asia, https://doi.org/10.1594/PANGAEA.891416, 2018b.

Sakai, A.: GAMDAM glacier inventory for High Mountain Asia: Area–altitude distribution for South Asia East, https://doi.org/10.1594/PANGAEA.891417, 2018c.

Sakai, A.: GAMDAM glacier inventory for High Mountain Asia: Area–altitude distribution for South Asia West, https://doi.org/10.1594/PANGAEA.891418, 2018d.

Sakai, A.: GAMDAM glacier inventory for High Mountain Asia: Central Asia in ArcGIS (shapefile) format, https://doi.org/10.1594/PANGAEA.891419, 2018e.

Sakai, A.: GAMDAM glacier inventory for High Mountain Asia: North Asia in ArcGIS (shapefile) format, https://doi.org/10.1594/PANGAEA.891420, 2018f.

Sakai, A.: GAMDAM glacier inventory for High Mountain Asia: South Asia East in ArcGIS (shapefile) format, https://doi.org/10.1594/PANGAEA.891421, 2018g.

Sakai, A.: GAMDAM glacier inventory for High Mountain Asia: South Asia West in ArcGIS (shapefile) format, https://doi.org/10.1594/PANGAEA.891422, 2018h.

Sakai, A. and Fujita, K.: Contrasting glacier responses to recent climate change in high-mountain Asia, Sci. Rep., 7, 13717, https://doi.org/10.1038/s41598-017-14256-5, 2017.

Shannon, S., Smith, R., Wiltshire, A., Payne, T., Huss, M., Betts, R., Caesar, J., Koutroulis, A., Jones, D., and Harrison, S.: Global glacier volume projections under high-end climate change scenarios, The Cryosphere, 13, 325–350, https://doi.org/10.5194/tc-13-325-2019, 2019.

Supplement of

Brief Communication: Updated GAMDAM Glacier Inventory over the High Mountain Asia

Akiko Sakai[1],

Correspondence to: Akiko Sakai (shakai@nagoya-u.jp)

Table S1. List of Landsat scenes used to delineate glacier outlines. attached ' TableS1_gamdam.xls'

Table S2. Summary of total glacier area in each region of the GGI18, GGI15 and RGI6.0.

	GGI18 (km^2)	GGI15 (km2)	RGI6.0 (km^2)	Difference (%) $\frac{(GGI18-GGI15)}{GGI15}$	Difference (%) $\frac{(GGI18-RGI6.0)}{RGI6.0}$
CentralAsia	50,519 ± 6,292	44,632 ± 6,695	49,302	13	2.5
SouthAsiaEast	15,895 ± 2,002	13,480 ± 2,022	14,734	18	7.9
SouthAsiaWest	33,034 ± 3,309	28,356 ± 4,253	33,568	16	-1.6
NorthAsia*	1,244 ± 188	1,114 ± 167	1,163	12	7.0
Total	100,693 ± 11,790	87,583 ± 13,137	98,767	15	2.0

*: Only Altay and Sayan

Table S3. Area comparison between the GGI18 limited to the NM18 domain and NM18 and between the GGI18 limited to the CGI2 domain and CGI2. Both overlapping areas and overlapping ratios are also listed.

**: This value includes glaciers of the first Chinese glacier inventory, where we have no glacier polygon in CGI2.

Name of inventory	GGI18 (NM18 domain)	NM18	GGI18 (CGI2 domain)	CGI2
Total area (km^2)	33,019±3,188	35,287±1,209	48,100±5,963	50563**
Overlapping area (km^2)	30,739		43,516	
Overlapping area ratio (%)	93 to total area of GGI18 limited at NM18 domain (= 33,019 km^2)	87 to total area of NM18 (= 35,287 km^2)	90 to total area of GGI18 limited at CGI2 domain (= 48,100 km^2)	86 to total area of CGI2 (= 50,563 km^2)

Table S4. List of Landsat scenes used to delineation tests. No. of scenes correspond to that of Fig. S4.

No.	Scene ID	Acquired date		
a	LT51400411995266BKT00	23	Sep	1995
b	LT51400411995282BKT00	9	Oct	1995
c	LT51400411998162BKT00	11	Jun	1998
d	LT51400411999117BKT00	27	Apr	1999
e	L71140041_04120001030	30	Oct	2000
f	LE71400412001290SGS00	17	Oct	2001
g	LE71400412001354SGS00	20	Dec	2001
h	LT51400412005149BKT00	29	May	2005
i	LT51400412009128KHC00	8	May	2009
j	LT51400412010163BKT01	12	Jun	2010

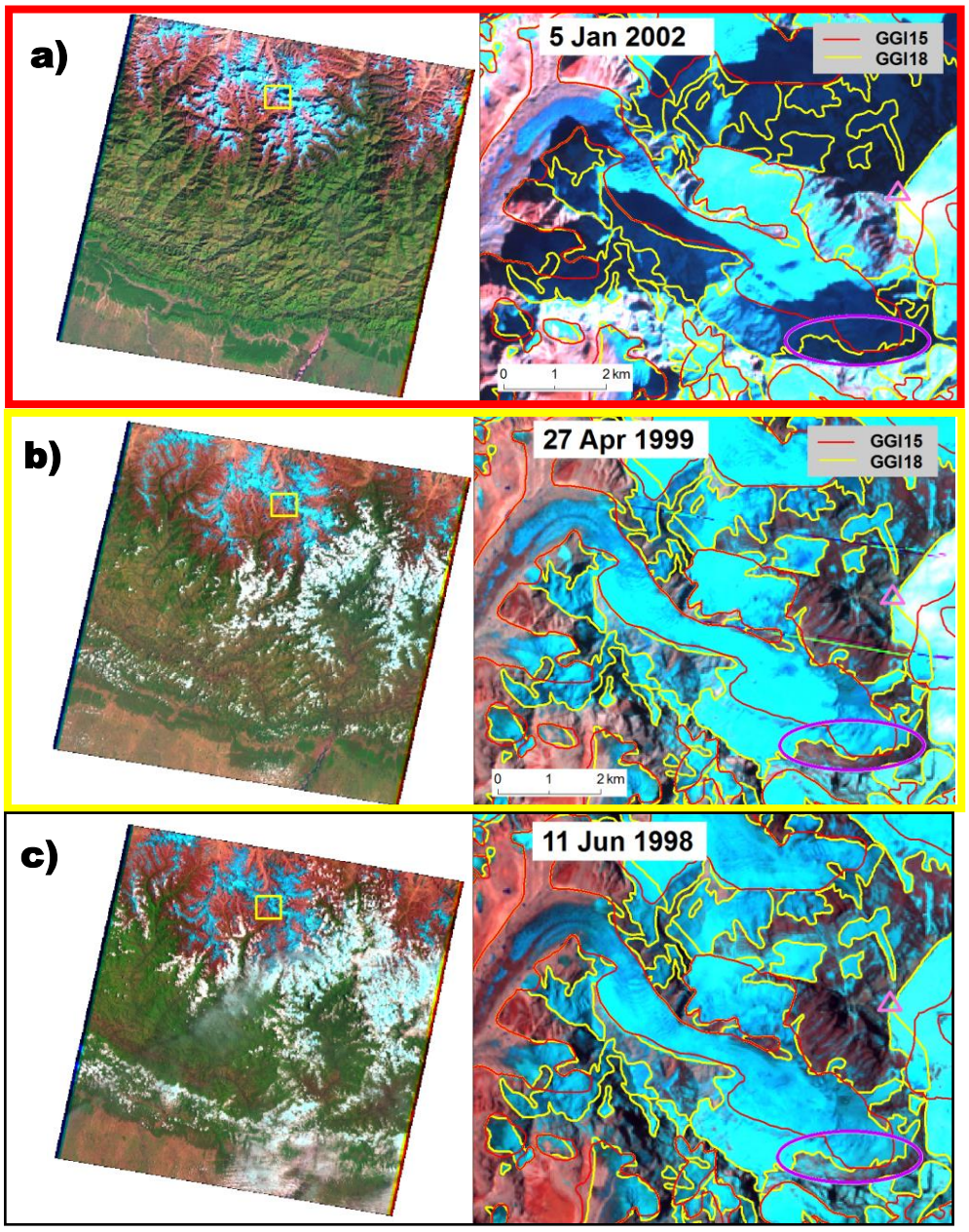

Figure S1: Example of selecting a Landsat scene for specific area. Left figures show the whole Landsat imagery with the location of the specific glacier (Khumbu Glacier) by yellow square. And right figures show accumulation area of the Khumb Glacier at 86°53'40.592"E 27°58'49.921"N (path140 row41 of WRS2) Date in the right figures indicate each acquisition date, and the peak of Mt. Everest (Qomolangma, Sagarmatha) are shown by a pink triangle. All images are false colour (bands 7, 4, and 2 as RGB) composite Landsat images. Glacier outlines are delineated using image taken in 2005 Jan 5 in the GGI15, but glacier area are shadowed and there are much seasonal snow a). In the process of revision, four images emerged as a candidate because they have less snow and no cloud at Khumbu Glacier b) and c). And image b) was selected due to clear outline at north-facing walls (purple ellipse) comparing to other images c).

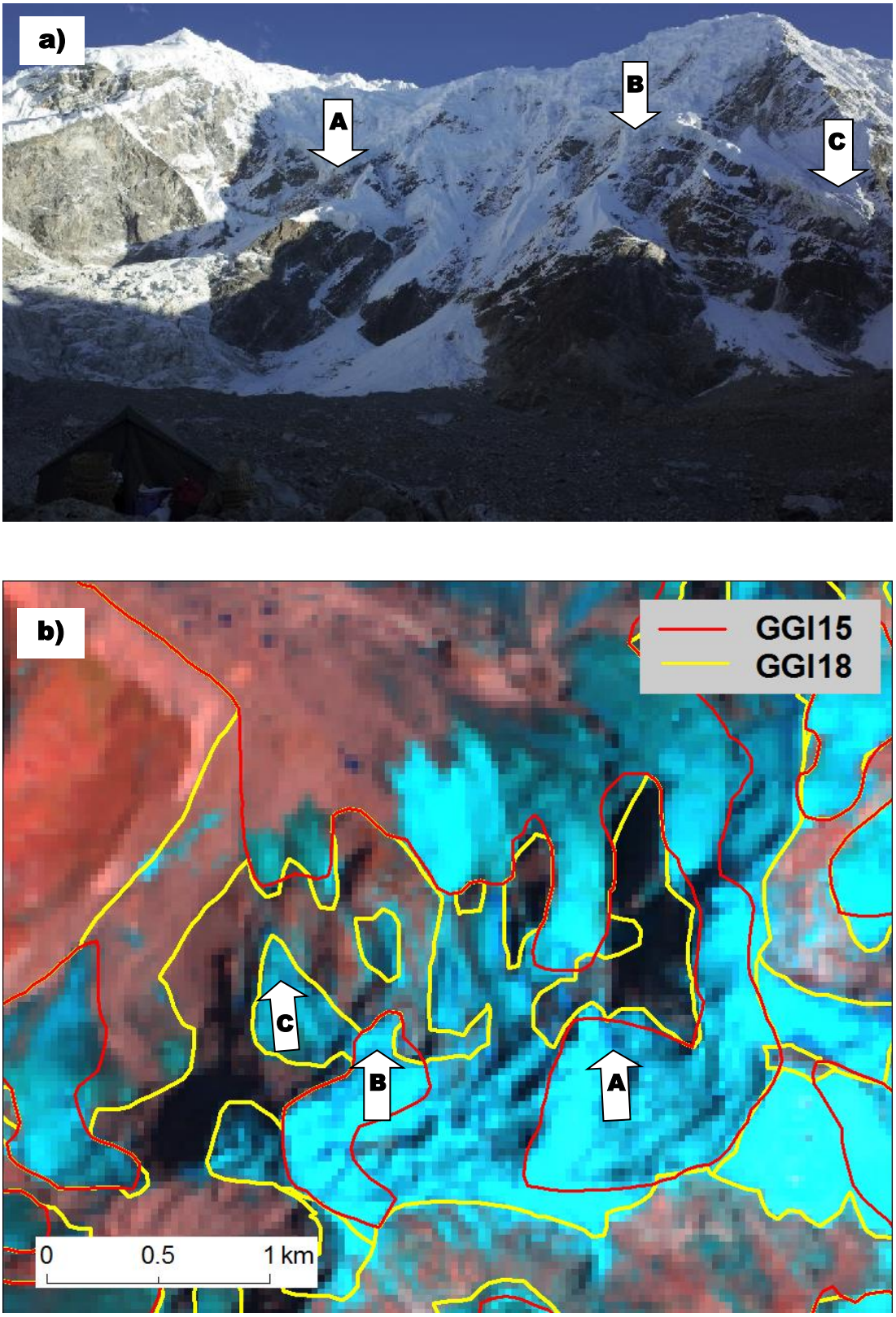

Figure S2: Glaciers at steep headwalls taken at the Trakarding Glacier (86°31'58.441"E 27°49'6.253"N path 140 row 41) in 2016 a), and the glacier outline b). Arrows from A to C indicate relatively thick hanging glaciers in a), each location correspond with those A to C in b). The background images of b) are false colour (bands 7, 4, and 2 as RGB) composite Landsat images taken on 27 Apr 1999.

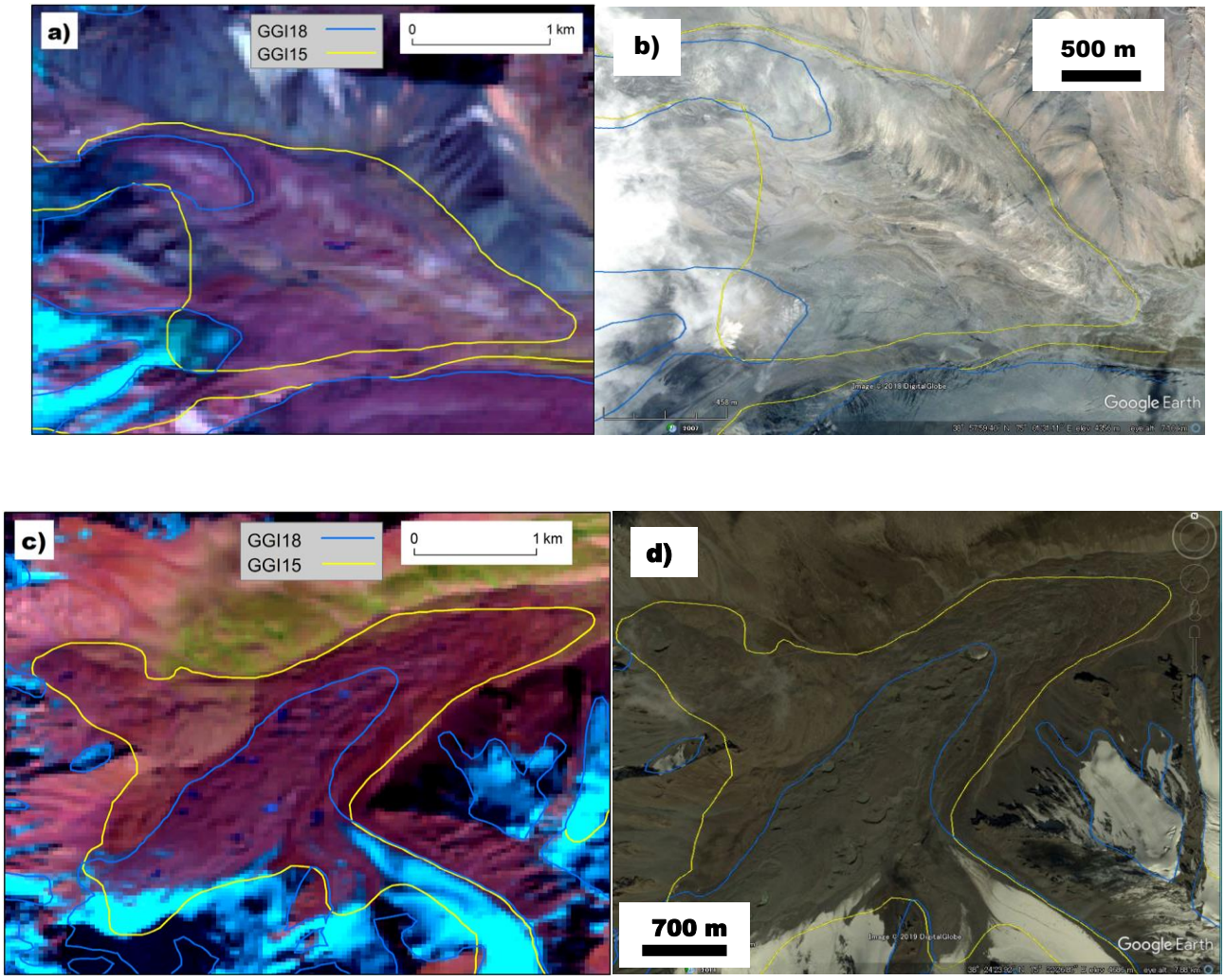

Figure S3: Example of excluded rock glacier-like geography in GGI18 at 75°1'55.261"E 38°57'22.842"N (path149 row33 of WRS2) a) and b), and at 75°23'9.322"E 38°23'47.306"N (path149 row33 of WRS2)c) and d). The background images are false colour (bands 7, 4, and 2 as RGB) composite Landsat images taken on 25 Sep 1999 a) c), Google Earth images on 4 July 2007 b), on 21 Aug 2011c), respectively.

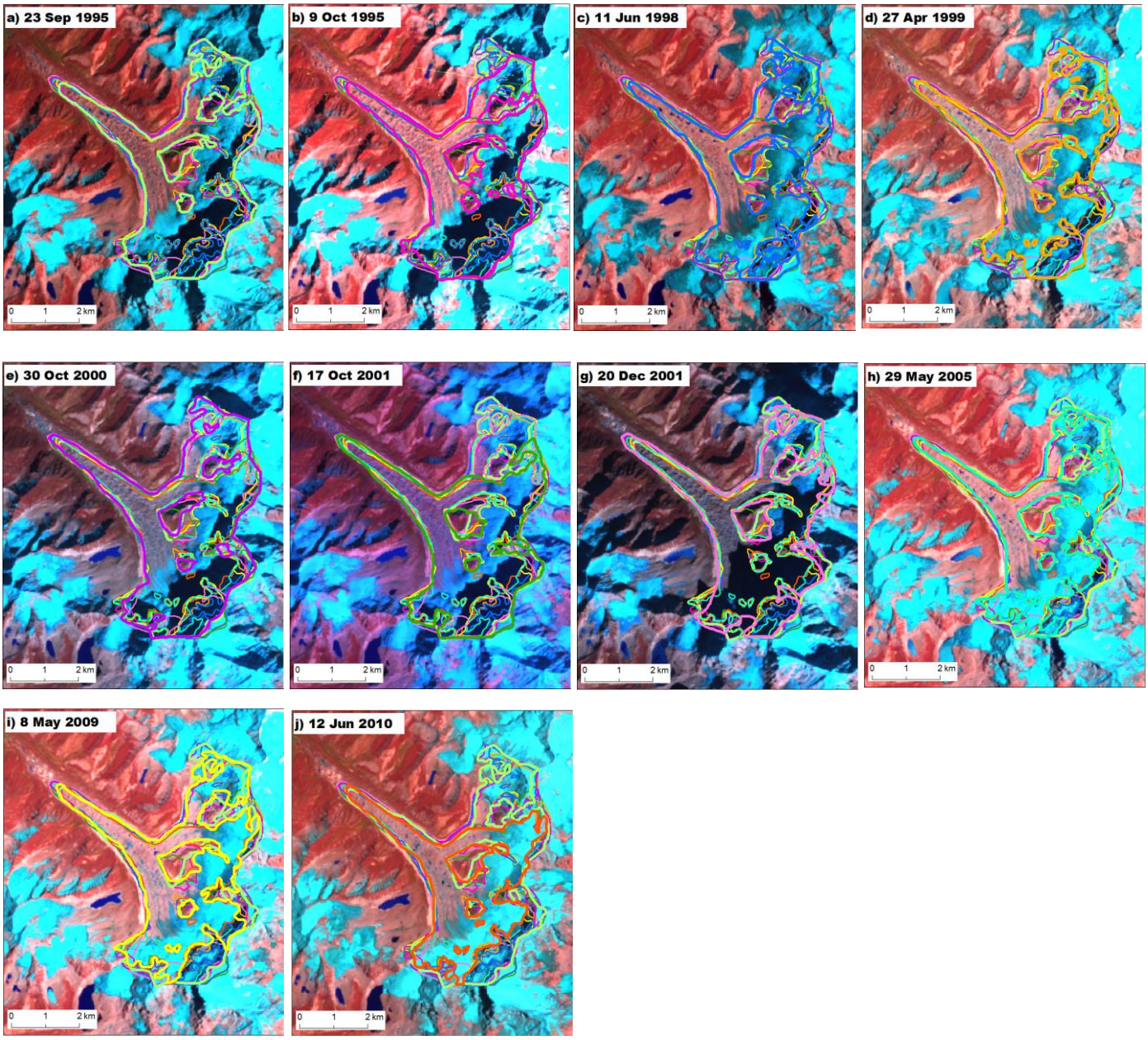

Figure S4: One example of delineation tests (86°31'52.046"E 28°5'7.04"N) to calculate normalised standard deviation of debris-covered glacier area (Fig. S5). Delineation test were carried out using 10 Landsat imageries at path140 row41 of WRS2, which information are listed in Table S4. One polygon were made for each imagery as shown by thick color lines. The backgrounds are false colour (bands 7, 4, and 2 as RGB) composite Landsat images. Each acquisition date were shown in each figure.

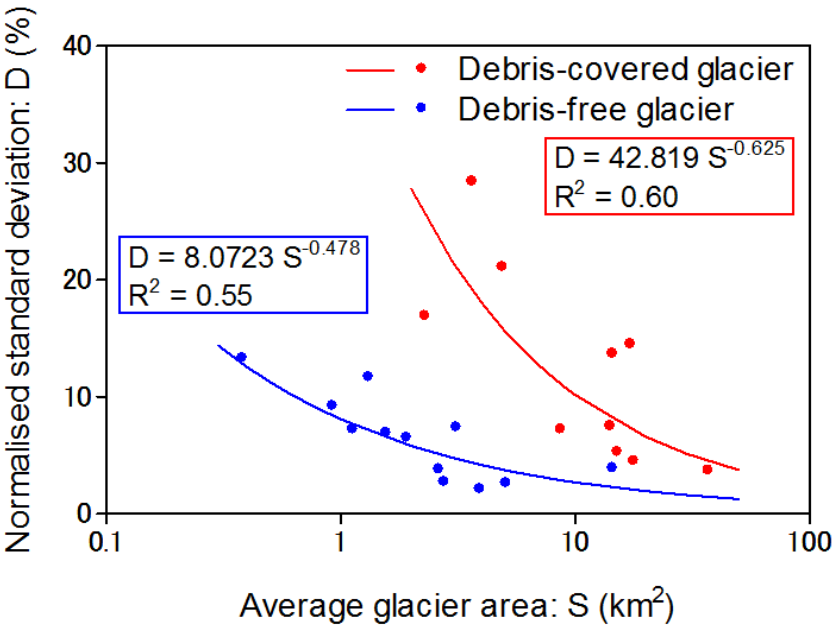

Figure S5: Normalised standard deviation of glacier area at each mean glacier area. Normalised standard deviation of glacier area are calculated standard deviation of glacier area based on delineations using 10 Landsat imageries divided by the mean glacier area for 10 debris-covered glaciers and for 12 debris-free glaciers.

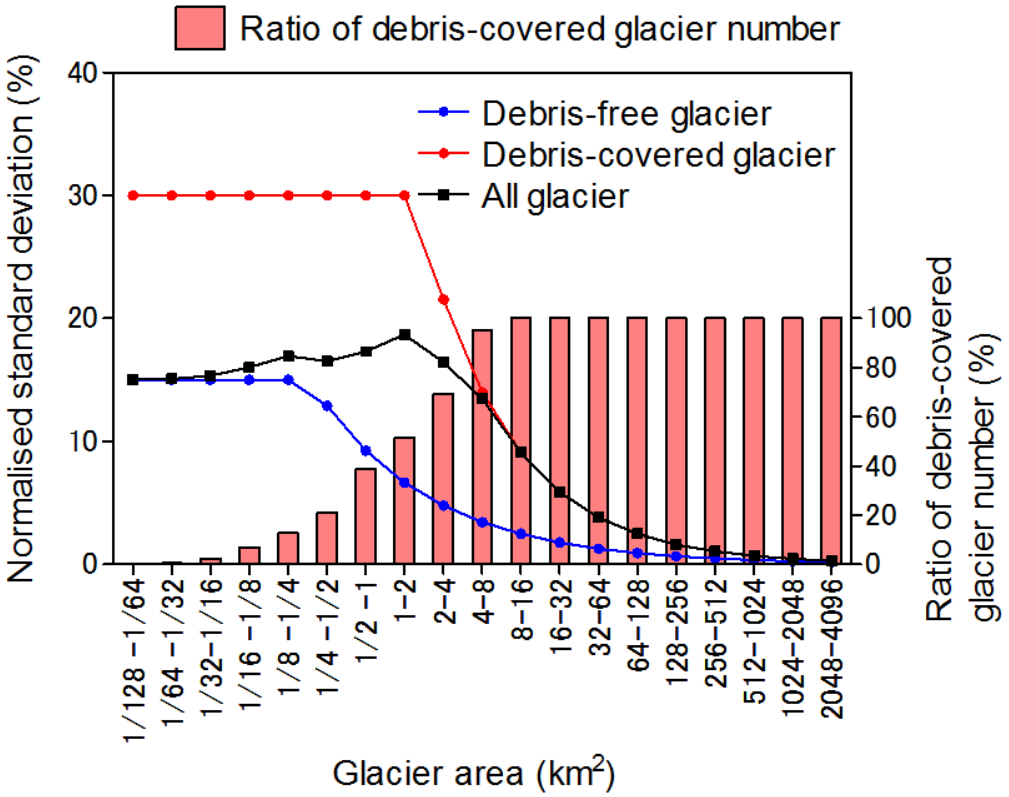

Figure S6: Normalised standard deviation (NSD) of glacier area and ratio of debris-covered glacier number at each glacier area class. NSD of debris-covered glacier area and debris-free glacier area are derived from the regression lines in Fig. S2 assuming that the NSDs are 30% for smaller (< 2 km^2) debris-covered glacier and 15% for smaller (< 0.25 km^2) debris-free glacier. NSD of all glaciers are calculated from number weighted average of NSDs of debris-covered glacier area and debris-free glacier area.

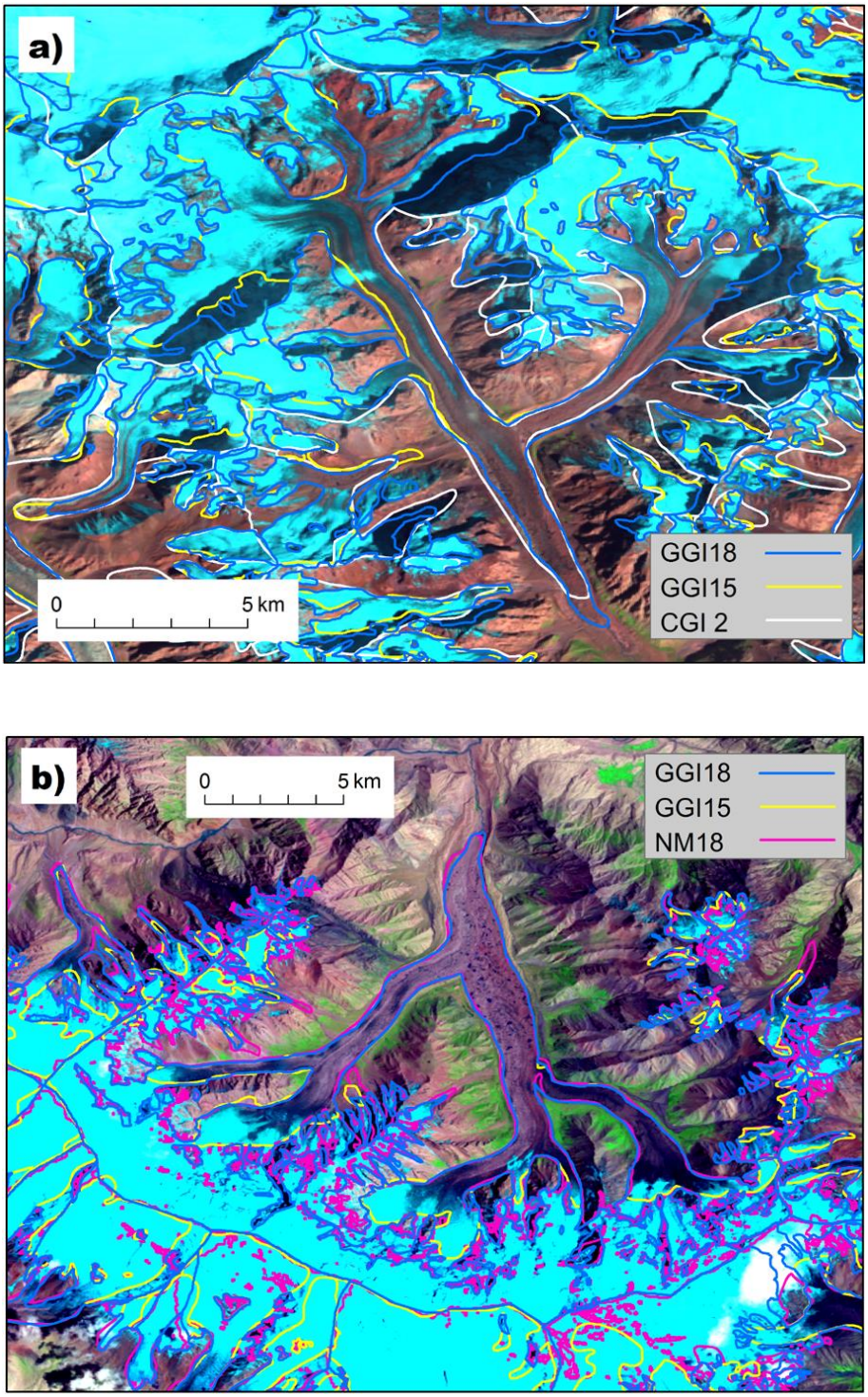

Figure S7: Comparison of the glacier outlines of each glacier inventory, GGI15, GGI18, and CGI2, at 80°21'36"E, 42°2'23"N (path147 row31 of WRS2) a). And comparison of GGI15, GGI18, and NM18, at 75°17'11"E, 38°39'54"N (path149 row33 of WRS2) b). The backgrounds are false colour (bands 7, 4, and 2 as RGB) composite Landsat images taken on 10 September 1996 (a), and 11 July 1994 (b), respectively.

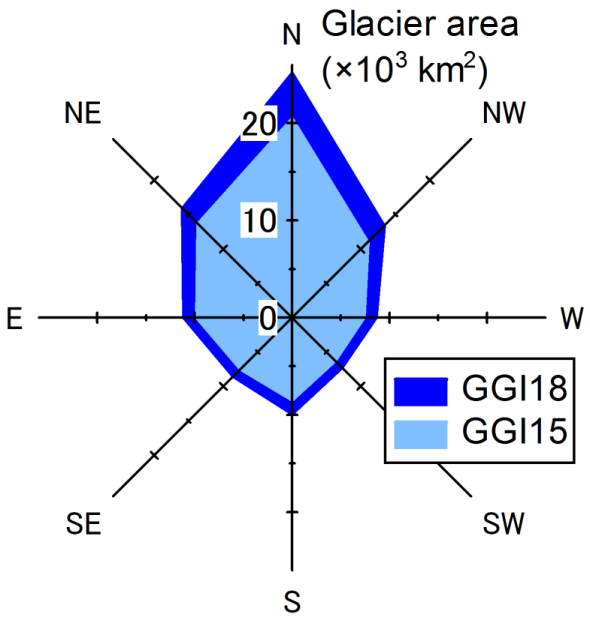

Figure S8: Glacier area distribution from different aspects with an interval of 45 degrees (eight azimuths). The area of aspect was calculated based on aspect of pixels in glacier polygons. Blue and light blue colours indicate the GGI18 and GGI15 for whole study regions, respectively.

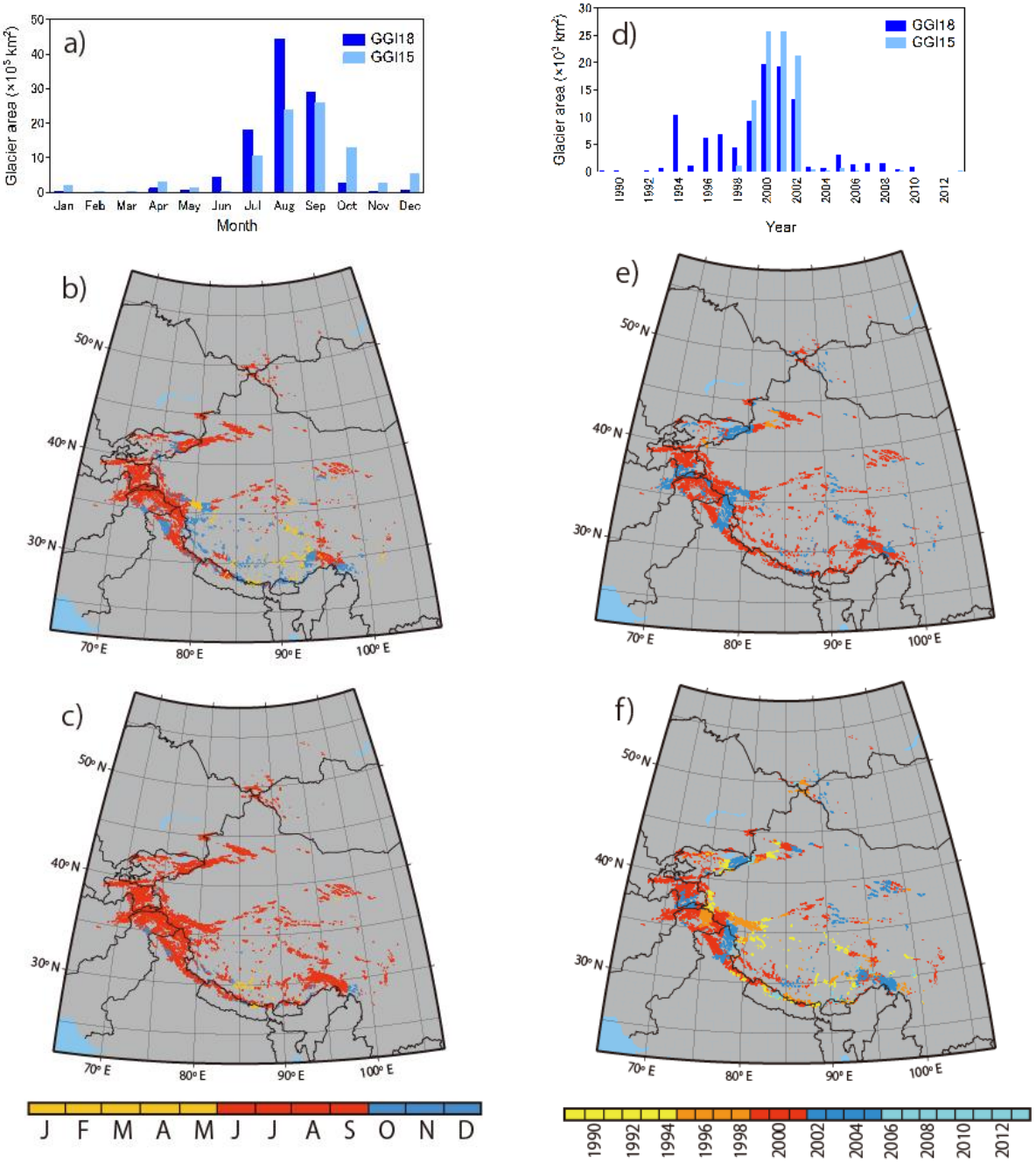

Figure S9: Frequency distribution of the acquisition month of the Landsat scenes used to delineate the glaciers in the GGI15 and GGI18 by glacierised area (a). Distribution of glacier area centre coloured by acquisition month in the GGI15 (b) and in the GGI18 (c). Frequency distribution of the acquisition year of the Landsat scenes used to delineate the glaciers in the GGI15 and GGI18 by glacierised area (d). Distribution of glacier area centre coloured by acquisition year in the GGI15 (e) and in the GGI18 (f).

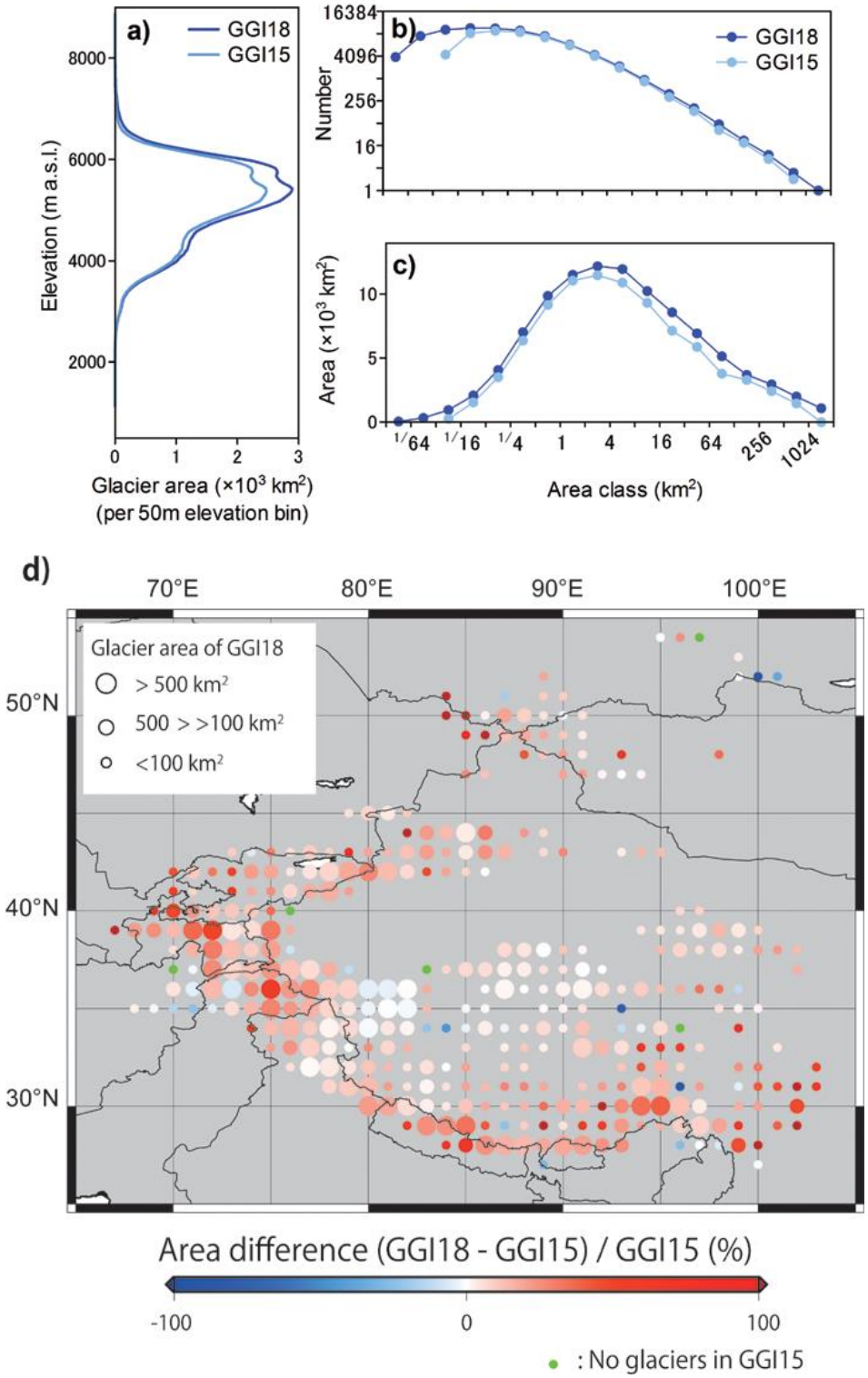

Figure S10: Comparison between the GGI15 and the GGI18. Each glacier hypsography a) at every 50-m elevation bin. Glacier number b) and total area c) at each area class. There is no data in the area class from 0.01 to 0.05 km^2 in the GGI15, because the minimum glacier area was set at 0.05 km^2. Glacier polygons were aggregated at each 1×1º grid based on center of each glacier polygon for each inventories for regional area difference between GGI15 and GGI18 d). The size of each circle indicates glacier area sum of GGI18 at each grid cell d).

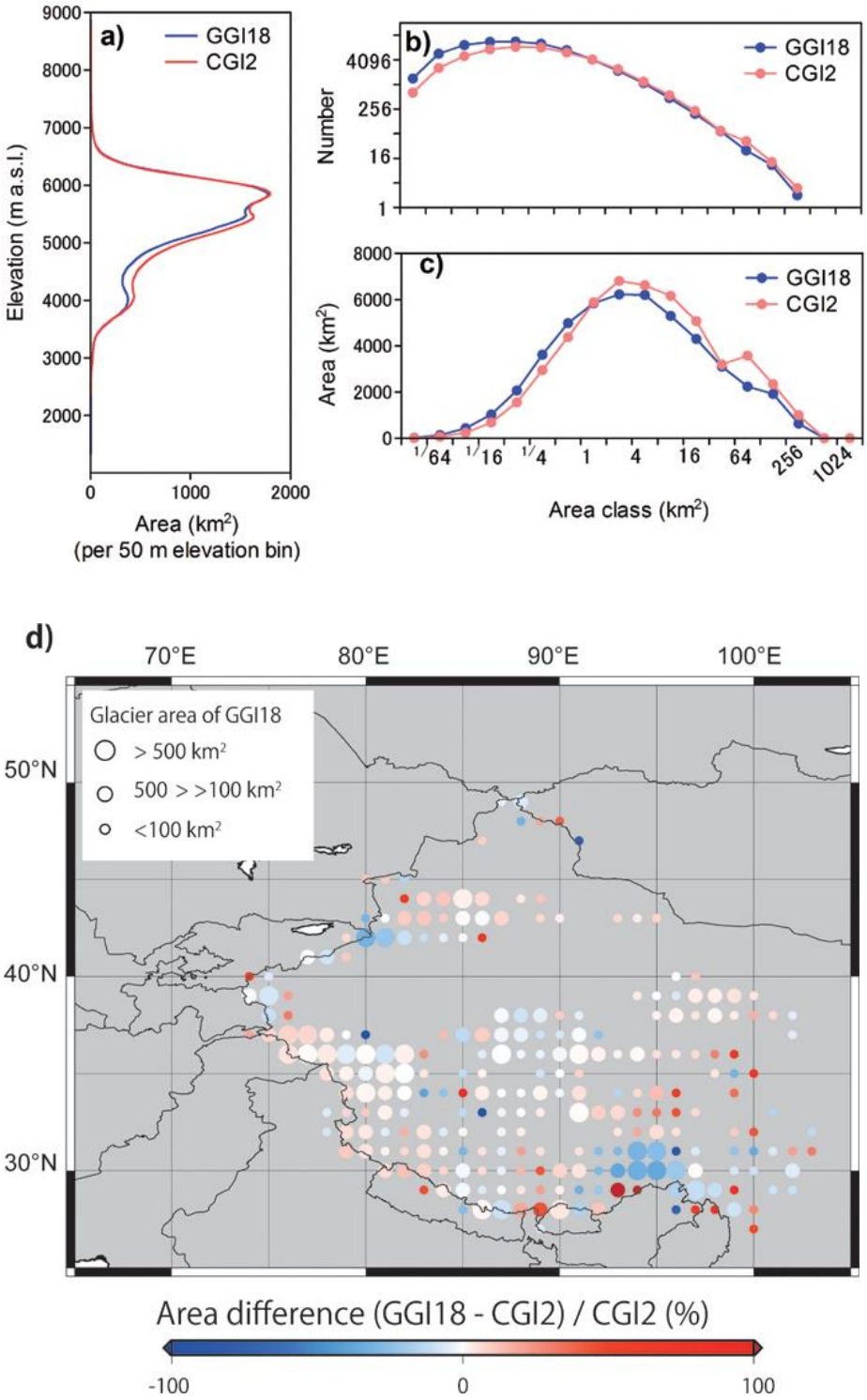

Figure S11: Comparison between the CGI2 and GGI18 limited to the CGI2 domain. Each glacier hypsography a) at every 50-m elevation bin. Glacier number b) and total area c) at each area class. Both inventories include only glaciers > 0.01 km^2 in area. Glacier polygons were aggregated at each 1×1º grid based on center of each glacier polygon for each inventories for regional area difference between CGI2 and GGI18 d). The size of each circle indicates glacier area sum of GGI18 at each grid cell d).

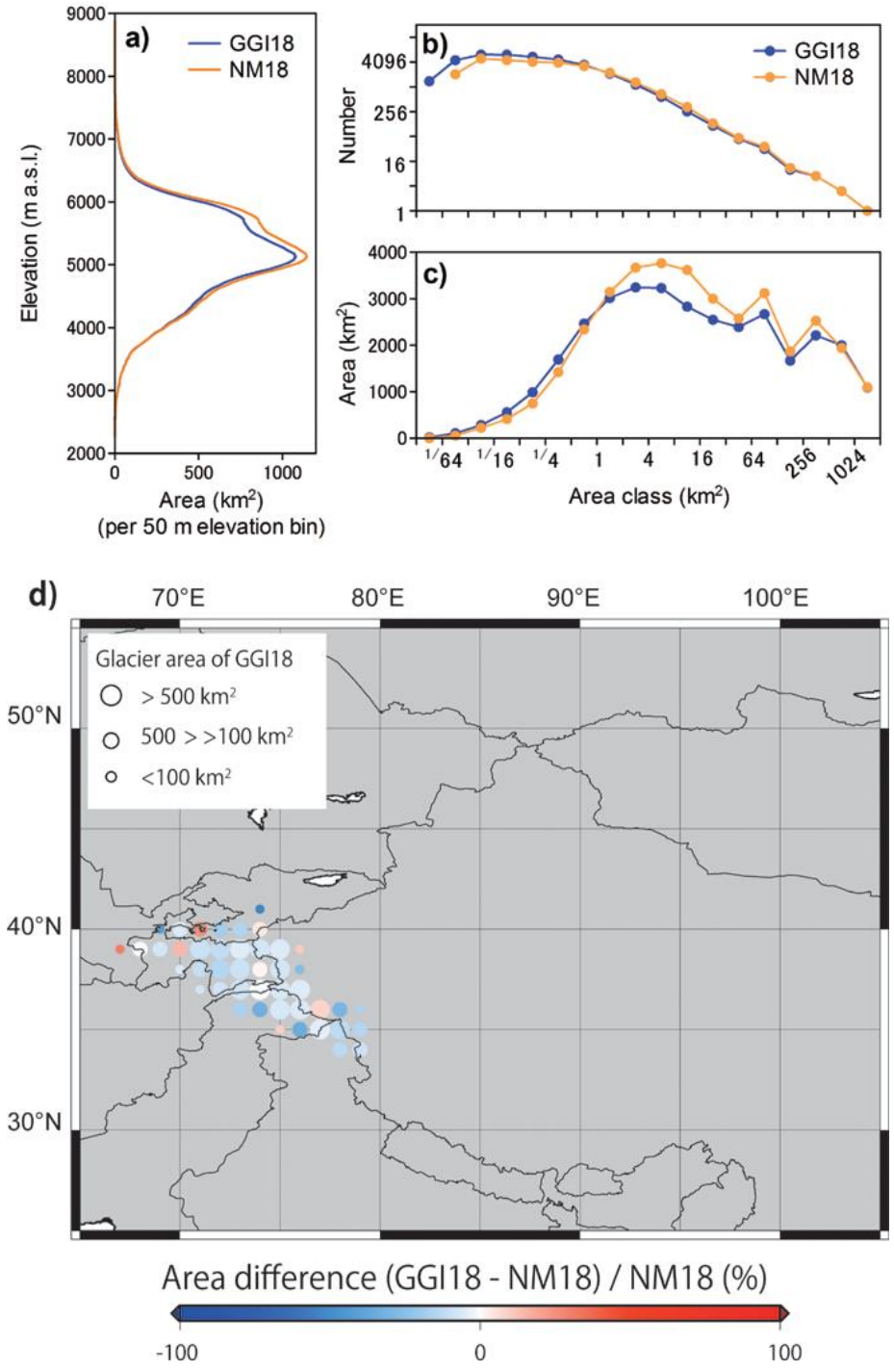

Figure S12: Comparison between the NM18 and GGI18 limited to the NM18 domain. Each glacier hypsography a) at every 50-m elevation bin. Glacier number b) and total area c) at each area class. There is no data in the area class from 0.01 to 0.02 km^2 in NM18 because only glaciers > 0.02 km^2 in the area were included. Glacier polygons were aggregated at each 1×1º grid based on center of each glacier polygon for each inventories for regional area difference between NM18 and GGI18 d). The size of each circle indicates glacier area sum of GGI18 at each grid cell d).

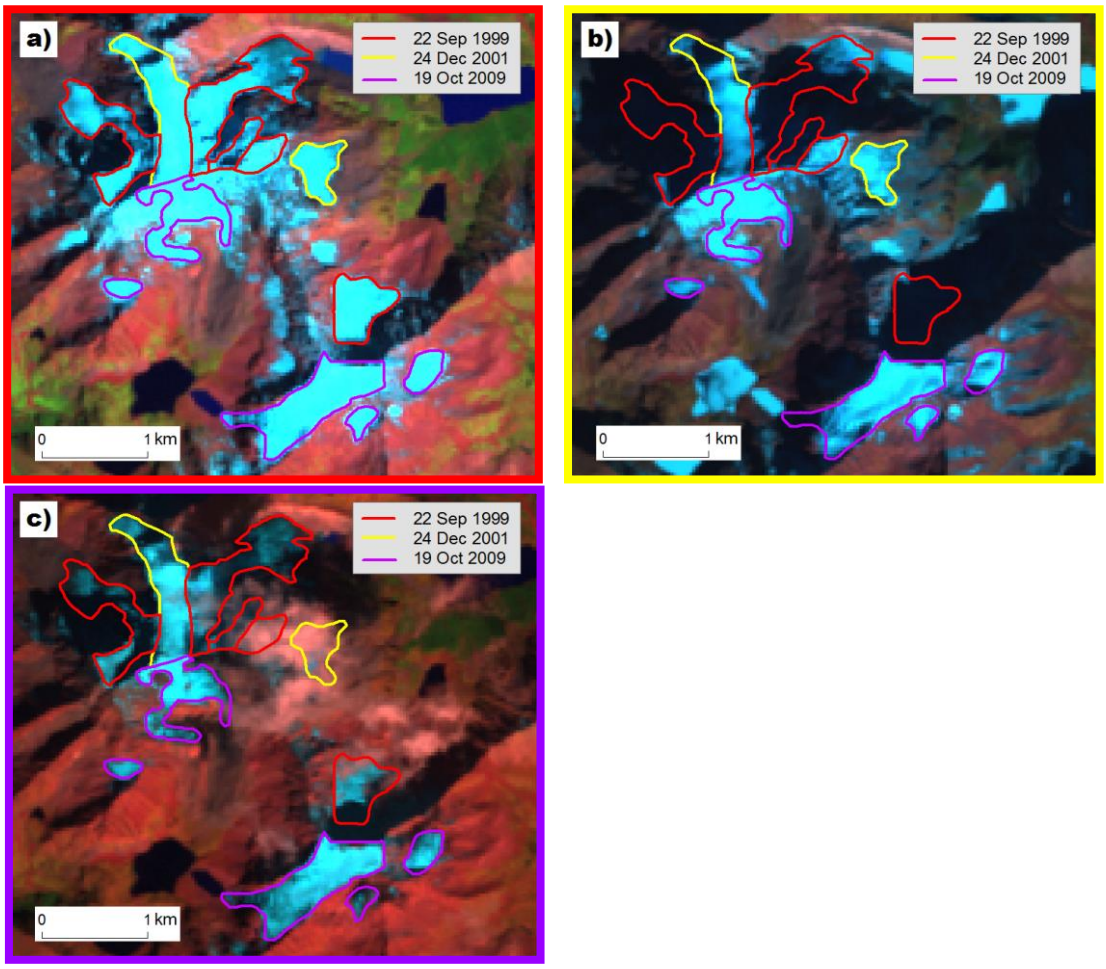

Figure S13: Example of delineation of glaciers using multiple Landsat scenes in GGI18 at 93°31'57.747"E 29°37'1.678"N (path136 row40 of WRS2). Each color of glacier outlines were digitized based on Landsat scenes framed by each corresponding colour. In this East Himalaya Mountain region, quality of glacier outlines are very low, since the cloud cover, seasonal snow and shadow hamper to delineate the glacier area. Then, I have to delineate glaciers through wisps of cloud and also cannot avoid using winter imageries. The background images are false colour (bands 7, 4, and 2 as RGB) composite Landsat images taken on 22 Sep 1999 a), 24 Dec 2001 b) and 19 Oct 2009 c), respectively.